Paper Title: Thermal characterization of full-scale PCM products and numerical simulations, including hysteresis, to evaluate energy impacts in an envelope application

Authors: Kaushik Biswas[1], Yash Shukla[2], Andre Desjarlais[1] and Rajan Rawal[2]

Author Affiliations:
[1] Oak Ridge National Laboratory, One Bethel Valley Road, Oak Ridge, TN 37831, USA
[2] Center for Advanced Research in Building Science and Energy, CEPT University, K.L. Campus, Navarangpura, Ahmedabad 380009, India.

Corresponding Author:
Kaushik Biswas, Ph.D.
One Bethel Valley Road, Building 3147
P.O. Box 2008, M.S. - 6070
Oak Ridge, TN 37831
Ph: +1 (865) 574-0917
Fax: +1 (865) 574-9354
Email: biswask@ornl.gov

ABSTRACT

This article presents combined measurements of fatty acid-based organic PCM products and numerical simulations to evaluate the energy benefits of adding a PCM layer to an exterior wall. The thermal storage characteristics of the PCM were measured using a heat flow meter apparatus (HFMA). The PCM characterization is based on a recent ASTM International standard test method, ASTM C1784. The PCM samples were subjected to step changes in temperature and allowed to stabilize at each temperature. By measuring the heat absorbed or released by the PCM, the temperature-dependent enthalpy functions for melting and freezing were determined.

The simulations were done using a previously-validated two-dimensional (2D) wall model containing a PCM layer and incorporating the HFMA-measured enthalpy functions. The wall model was modified to include the hysteresis phenomenon observed in PCMs, which is reflected in different melting and freezing temperatures of the PCM. Simulations were done with a single enthalpy curve based on the PCM melting tests, both melting and freezing enthalpy curves, and with different degrees of hysteresis between the melting and freezing curves. Significant differences were observed between the thermal performances of the modeled wall with the PCM layer under the different scenarios.

Keywords: PCM characterization; heat flow meter apparatus; ASTM C1784; PCM hysteresis modeling; 2D wall model with PCM

NOMENCLATURE

Bi	Biot number
C_p	Specific heat (J/kg/K)
F	View factor
H	Enthalpy (J/g)
h	Convective heat transfer coefficient (W/m^2/K)
k	Thermal conductivity (W/m/K)
N	Number of readings in a HFMA block
Q	Energy released/absorbed per unit area by the PCM (J/m^2)
q	Heat flux (W/m^2)
q_{solar}	Solar irradiance (W/m^2)
R	Radius of tube used in T-history method (m)
S	HFMA plate calibration factor ((W/m^2)/mV)
T	Temperature (K)
V	Voltage signal from HFMA plates (mV)
x	Thickness (m)
ΔH	Step-wise enthalpy change (J/g)
ΔT	Temperature step change in HFMA plates (K)
δx	HFMA plate thickness (m)
α	Solar absorptance
β	Term used in view factor calculation
ε	Infrared emittance
ϕ	Inclination of the modeled wall with the ground
ρ	Density (kg/m^3)
τ	Time period of each HFMA reading (1.3 s)

Subscripts:

equi.	Equilibrium condition of the HFMA
ext	Exterior
int	Interior
L	Lower plate of the HFMA
l	Fully molten state of PCM
s	Fully frozen state of PCM
U	Upper plate of the HFMA

Abbreviations:

COP	Coefficient of performance

HFMA	Heat flow meter apparatus
LWR	Long wave radiation
OSB	Oriented strand board
PCM	Phase change material
TMY	Typical meteorological year

1. INTRODUCTION

Phase change materials have garnered a lot of attention for applications in building envelopes for energy storage, reducing cooling loads and peak load shifting, and improving comfort conditions [1-3]. In order to accurately evaluate the performance of a PCM-based system, the knowledge of the main thermophysical properties of the selected PCM is important [4-6]. The thermal storage characteristics of a PCM are well-defined via four parameters, the specific heats in the solid and molten phase, melting temperature and the phase change enthalpy [7]. However, most PCMs exhibit a melting range instead of a single melting temperature, in which case the shape of the enthalpy curve as a function of temperature [*H(T)*] describes the material with much better precision [7].

Differential scanning calorimetry (DSC) is one of the most-commonly used methods for determining the enthalpy function of PCMs and its application to PCMs has been described in the literature [7, 8]. The DSC method assumes isothermal conditions within the test sample (PCM) and this requirement limits the samples to very small sizes (1-10 mg), which may result in the thermophysical properties of the test sample being different from those of the bulk material [4]. High heating and cooling rates can lead to temperature gradients within the PCM test sample and lead to measurement artifacts, such as the heating and cooling enthalpy curves being systematically shifted to higher and lower temperatures, respectively [7, 8].

Yinping et al. [4] introduced the T-history method for PCM characterization. In their method, the authors started with a tube containing a liquid PCM maintained at a temperature above its melting point and another with water at the same initial temperature, followed by exposing both samples to an ambient temperature lower than the phase change range of the PCM and measuring the temperature evolution of both samples. Using the known properties of water (or another standard material) and the test tube, the specific heats (solid and liquid) and the latent heat of the PCM could be determined [4]. Over the years, several researchers have proposed modifications and improvements to the T-history method [9-11]. The T-history method is purported to be a more suitable method for PCM characterization than DSC as it allows analysis of larger samples (15 g) with simpler equipment and in less time [12].

However, even with the T-history method the samples are limited in size and shape compared to what might be expected with PCM products for building envelopes. T-history method is based on the lumped capacitance method, i.e. the temperature distribution in the sample is assumed to be uniform, which is reasonable if the Biot number ($Bi = hR/2k$) is less than 0.1; where 'R' is the radius of a tube, 'k' the thermal conductivity of the PCM and 'h' the natural convective heat-transfer coefficient of air outside the tube [4]. To ensure the validity of the lumped capacitance approach, typically test tubes of a small diameter are used as containers for the PCM [13].

Recently, a new ASTM International standard called ASTM C1784 [14] has been established to enable measurements of PCMs as well as inhomogeneous building products containing PCMs. Several different forms of PCM-based building products have been reported in the literature, including shape-stabilized PCM sheets [15], PCM wallboards [16-18], PCM mixed in concrete and brick [19, 20], PCM-impregnated insulation materials [21-23], macro-packaged PCM in plastic pouches [24], and products with nano-PCM composites [25]. ASTM C1784 is based on a modified application of a heat flow meter apparatus (HFMA), which was originally designed according to the requirements of ASTM C518 [26] to measure steady-state thermal conductivity of materials. Shukla and Kosny [27] reported test data from several PCM-integrated products based on the new test method. The authors noted that the dynamic thermal properties of

PCM-integrated building products are dependent on parameters such as the fraction of PCM within the product as well as specific heat and thermal conductivity of all the components [27]; the additional components might be packaging and additives such as fire retardants, conductivity enhancers, etc. Further, the properties of the PCM itself may change due to surrounding materials and introduction of foreign materials. Therefore, the properties of PCM- integrated components may be significantly different than ones derived from the pure PCM [27]. Kim et al. [15] used a variation of the heat flow meter method to measure specific heats of PCM sheets in a thermostatic chamber. The chamber temperature was raised or lowered by 1˚C every 30 minutes over the range of the PCM transition temperatures, with 4 hours of stabilization period between heating and cooling tests. The specific heats were calculated using the measured heat flows and rate of change of temperature [15]. PCM products that have been tested using heat flow meters include PCM-enhanced gypsum board, PCM-aerogel composite, shape-stabilized PCM sheet, and PCM-enhanced blown cellulose [15, 27].

Regarding numerical modeling of building envelopes with PCMs, AL-Saadi and Zhai [28] reviewed the literature and classified the models into three categories based on their level of complexity: simple, intermediate and sophisticated models. The authors compared the different models in terms of their advantages and disadvantages regarding simulation capabilities for complex systems and computational efficiency. The authors noted that many existing models ignore hysteresis and subcooling that are inherent in some PCMs and cannot be used for annual simulations of building thermal performance with PCMs [28]. Bony and Citherlet [29] defined hysteresis as a delay in phase change while cooling, i.e. the freezing begins at a lower temperature than the end of the melting phase. Paraffinic PCMs exhibit very little hysteresis (~1˚C or less) [8, 18], while organic bio-based PCMs and inorganic salt hydrates can exhibit hysteresis of 5-13˚C [24, 30].

Kuznik and Virgone [31] showed the need to model thermophysical property curves of both melting and freezing to account for hysteresis. The authors used specific heats (C_p) from melting and freezing curves in separate models and compared the results against experimental data from heating and cooling steps. The model with the melting 'C_p' yielded good match with melting step data and freezing curve-based model matched well with cooling step data, but not vice-versa [31]. Gowreesunker and Tassou [32] utilized varying enthalpy–temperature relationships during melting and freezing in a computational fluid dynamics (CFD) model to study the effects of PCM clay boards on the control of indoor environments. When validated against experimental measurements of indoor temperatures, the model utilizing the separate melting and freezing enthalpy functions showed better simulation accuracy than a model using a single, idealized linear enthalpy function [32].

Researchers have used different methods of incorporating separate enthalpy curves for melting and freezing in models, specifically the treatment of interrupted melting or freezing. In other words, what if the PCM is subjected to heating while its state is defined by the freezing curve or vice-versa? One method is to assume enthalpy transitions from one curve to the other at a slope equal to the slope of the enthalpy curve in the solid phase [29, 33] or a horizontal transition between the curves [34]. Another method is to assume no transitions, i.e. the PCM state remains on the same curve whether heating or cooling and only transitions to the other curve once the melting end temperature has been exceeded (melting to freezing curve transition) or if the temperature falls below the freezing end temperature (freezing to melting curve transition) [33, 35].

The current work presents measurements of melting and freezing enthalpy curves of two

PCMs using the HFMA and estimations of annual energy performance using a two-dimensional (2D) model of a PCM-enhanced wall system. To the authors' knowledge, this is the first study that combines measurements of full-scale PCM products with annual energy simulations using a 2D wall model incorporating the hysteresis in PCMs. The current model is based on an existing wall model that was validated against data from experiments on a full-scale wall system with a PCM wallboard and then used to calculate the annual energy impacts of the PCM wallboard [18]. The existing model was modified to include an 8.3 mm layer of PCM (instead of the PCM wallboard) and to incorporate the PCM hysteresis. Interrupted heating and cooling cycles were treated without instantaneous transitions from one curve to the other, following [33, 35].

2. PCM THERMAL CHARACTERIZATION USING HFMA

2.1. Description of HFMA

Figure 1 shows a heat flow meter apparatus (HFMA). The HFMA used in this study is one of the Fox 300 models, similar to the current Fox 314 from TA Instruments [36]. The apparatus consists of upper and lower plates, which sandwich the test specimen. Each plate is outfitted with a solid state heating and cooling system and the plate temperatures can be independently controlled to induce a heat flow in either upward or downward direction through the specimen. Thin-film heat flux transducers (HFTs), of dimensions 7.6 x 7.6 cm and thickness 1.78 mm, are permanently bonded to the upper and lower plate surfaces. Each plate contains one HFT installed at the center of the plate. In the center of the each transducer, a Type E thermocouple is bonded near its surface, close to the test specimen. These thermocouples accurately measure the specimen surface temperatures and are also used to control the plate temperatures.

During tests, a set of data is taken once every 1.3 seconds. Each set of data includes the upper and lower plate temperatures and heat flux transducer outputs. 512 consecutive sets of data are organized in one block and are averaged to yield the mean plate temperatures and heat fluxes. The following thermal equilibrium criteria need to be met for a test to be considered complete:

1. The block average temperature of each plate must be within 0.2K of the previous block.
2. The difference between the average HFT voltages from successive blocks must be within a certain absolute value (typically 50 mV) and within 2% of the earlier block average.

An additional criterion for test completion is the absence of any monotonic trends in the data. Once a certain number of consecutive blocks satisfy all equilibrium criteria, the test for a given temperature set point is considered complete. The HFMA is calibrated using a National Institute of Standards and Technology (NIST)-traceable standard reference material (SRM) 1450 [37] to convert the voltage signal to heat fluxes. With the measured sample thickness, upper and lower plate temperatures and heat fluxes, the thermal conductivity of the test specimen can be calculated.

2.2. PCM characterization

A modified application of the HFMA is to measure specific heats of materials [38]. The procedure involves measuring the amount of heat flow per unit area (Q, J/m^2) absorbed or released by a test sample on switching the HFMA plate temperatures after they have achieved thermal equilibrium at one set point to another, till the plates achieve thermal equilibrium at the new set points. The measured heat absorbed or released is also corrected for the heat capacity of the HFMA plates. The volumetric specific heat (ρC_p, J/m^3/K) of the test sample is then determined by dividing the corrected heat absorbed/released by the measured sample thickness; ‘ρ’ (kg/m^3) and ‘C_p’ (J/kg/K) are the density and specific heat of the test sample. Eqs. 1 and 2 show the calculations of ‘Q’ and ‘ρC_p’.

$$Q = \sum_{i=1}^{N} \left[S_U \left(V_{U,i} - V_{U,equi.} \right) + S_L \left(V_{L,i} - V_{L,equi.} \right) \right] \tau \quad (1)$$

$$\rho C_p = \left(\frac{Q}{\Delta T} - C_p' \rho' 2 \delta x' \right) / x \quad (2)$$

In the above equations, ‘N’ is the number of blocks, each with 512 readings, ‘S’ is the plate calibration factor ((W/m^2)/mV) , ‘V’ is the block-averaged voltage signal (mV), ‘τ’ is the time period for each data point (1.3 s), ‘ΔT’ is the temperature step change imposed on the HFMA plates, ‘$C_p' \rho' 2 \delta x'$’ is the plate correction factor (J/m^2/K), ‘$\delta x'$’ is the plate thickness (m), and ‘x’ is the sample thickness (m). The subscripts ‘U’ and ‘L’ represent the upper and lower plates, and ‘*equi.*’ represents the residual signals at the final equilibrium condition.

This additional capability of the HFMA can be utilized to measure the thermal storage characteristics of PCMs and led to the development of ASTM C1784 [14]. This test method makes a series of measurements to determine the thermal energy storage in a test specimen, or the enthalpy function, over a temperature range, as depicted in Figure 2. ‘T’ represents the plate temperatures and ‘Q’ is the energy released/absorbed by the PCM during the temperature steps. First, both HFMA plates are held at the same constant temperature until thermal equilibrium is achieved. Equilibrium is defined by the reduction in the amount of energy flow between the plates and the specimen to a very small (residual) and nearly constant value. Next, both plate temperatures are changed by identical amounts and held at the new temperature until equilibrium is again achieved. The energy absorbed or released by the specimen is recorded from the time of the temperature change until reaching equilibrium is again achieved. Using a series of temperature step changes and the measured thickness and density of the PCM, the step-wise enthalpy changes (ΔH, J/g) and cumulative enthalpy function ($H(T)$, J/g) over the PCM transition temperature range can be determined. Complete details of the test method are provided in ASTM C1784 [14].

2.3. Selected PCMs for characterization

Two PCM products were measured, SaveE® FS21R and SaveE® FS29, produced by PLUSS Advanced Technologies (http://www.pluss.co.in/). FS21R and FS29 have nominal melting temperatures of 20.7 and 29 ˚C, respectively, and are designed to yield latent heat capacities of 183 and 158 J/g. Both PCMs are blends of fatty acid-based organic materials in a polymer matrix. The PCMs are made into tiles that are encapsulated with a polyethylene layer and a thin aluminum foil (<0.5 mm); two layers are intended to reduce the risk of rupture. Further, the PCMs are designed to be form stable to minimize leakage even if the tiles are ruptured during installation. The form-stability also allows developing PCM tiles of different dimensions (thickness and shape) according to the application requirements.

The current PCM samples are about 30.5 x 30.5 cm in dimensions, 8 to 8.3 mm thick and weighed about 0.6 kg. One of the PCMs, FS21R, is shown in Figure 3. The PCM dimensions are deemed large enough to be representative of actual PCM products for building envelope applications; in fact, PCM tiles of the same dimensions were used in the ceiling of a test hut for a different study. The measurements were done in a HFMA with a 7.6 x 7.6 cm measurement area. The authors have access to a HFMA with a measurement area of 25.4 x 25.4 cm, which is being upgraded to add the specific heat measurement capability. A comparison of enthalpy measurements from the smaller and larger HFMA will provide insights about the uniformity of the PCM composition and if a larger measurement area or larger samples are required.

3. NUMERICAL SIMULATIONS

3.1. Model geometry and details

Simulations were performed using the heat transfer module of COMSOL Multiphysics® [39]. The current wall model, shown in Figure 4, is a modification of previous models that were validated against experimental data from tests of full-scale walls containing PCMs under real building and weather conditions [18, 23]. Simulations were performed with and without an 8.3 mm PCM layer; the case without the PCM served as a baseline. FS21R was the PCM used in the simulations. Due to its design, the PCM sheet is added as a separate layer in the current model compared to a PCM wallboard (18) and PCM-impregnated cavity insulation (23) in the previous modeling studies. The wall construction used in the model was “2 x 4” stud construction, i.e. it contained wood studs of 3.8 cm x 8.9 cm, resulting in a cavity depth of 8.9 cm. The centerlines of the studs were spaced 40.6 cm apart. The exterior side of the wall consisted of 1.3 cm oriented strand board (OSB) and the interior contained 1.3 cm gypsum wallboard. The cavity was filled with cellulose insulation. The modeled wall represents a typical construction practice for residential buildings in the United States (U.S.).

The model solved the following time-dependent energy equation:

$$\rho C_p \frac{\partial T}{\partial t} = \nabla \cdot (k \nabla T) \qquad (3)$$

In eq. 3, ‘T’ is the temperature, ‘ρ’ is the density, ‘Cp’ is the specific heat, and ‘k’ is the thermal conductivity of the different wall materials. Boundary conditions used in the model are described in section 3.3. Table 1 lists the material properties used in the numerical modeling.

These values were obtained from literature or through measurements. The conductivity measurements were done according to ASTM C518 [26].

Table 1. Material properties for numerical modeling

	Density (kg/m^3)	Thermal conductivity (W/m/K)	Specific heat (J/g/K)
Cellulose	40.8	0.042	1.424
Wood stud	576.7	0.144	1.633
OSB	640.0	0.130	1.410
Gypsum board	549.5	0.153	1.089
PCM (FS21R)	774.0	0.119(s)	--
		0.127 (l)	--

The thermal conductivities of the PCM were measured with HFMA plate temperatures that were both below or both above the phase transition range of the PCM. In other words, the conductivities were measured with the PCM in fully frozen and fully molten states, and the respective conductivities are represented by '*s*' and '*l*'. For simplicity of the simulations, and since the two measured conductivities were within 3% of the mean, an average value of 0.123 W/m/K was used in the simulations. The PCM specific heat ($C_{p,PCM}$) was calculated as the temperature derivative of the measured enthalpy functions (= dH/dT), using the hysteresis model described in section 3.2.

The scope of the study was limited to calculating heat flows through a 'clear' section of the wall, i.e. no features other than the wall cavity and stud were modeled. Wall-to-wall or wall-to-ceiling interfaces, joints and corners, windows, radiation exchange between interior surfaces, etc., were not considered in the model. Further, internal loads, solar gains and heat flows through windows, roof and ceiling loads, infiltration, etc. could not be considered due to the modeling limitations. Hence, only a small two-dimensional (2D) horizontal cross-section of the wall was modeled, extending from the stud centerline to the cavity centerline. Exterior boundary conditions were applied to the OSB surface that is exposed to the "outside" and an interior boundary condition was applied to the wallboard surface facing the interior conditioned space or "room". Symmetric boundary conditions were assumed at the stud and cavity centerlines, as indicated in Figure 4.

3.2. PCM hysteresis model

As described earlier, it is important to account for the hysteresis of PCMs for more realistic and accurate evaluations of PCM performance. Here, the hysteresis phenomenon in the PCM layer was modeled using a 'previous solution' operator in COMSOL [40].A variable named '*H_PCM*' was defined within the domain representing the PCM layer (see Figure 4). *H_PCM* is a binary variable that can take values of '0' and '1'. It should be noted that *H_PCM* does not define the state of the PCM as solid or liquid. Rather, depending on its value, the enthalpy curve of melting (*H_PCM* = 0) or freezing (*H_PCM* = 1) is used to calculate the specific heat of the PCM. The following equation was incorporated in the model:

$$H\_PCM - nojac\left[if\left\{T > T_{high}, 1, if\left(T < T_{low}, 0, H\_PCM\right)\right\}\right] = 0 \tag{4}$$

'T_{high}' is the temperature at which melting ends and 'T_{low}' is the freezing end temperature. According to eq. 4, at any location within the PCM layer, whenever the temperature from the previous solution step rose above T_{high}, that location was assumed to be fully molten, so *H_PCM* switched from "0" to "1" and the PCM enthalpy switched from the melting to the freezing curve. Conversely, at any location, if the temperature dropped below T_{low}, *H_PCM* switched from "1" to "0" and the PCM enthalpy switched to the freezing curve. For interrupted heating or cooling, the variable *H_PCM* retained its existing value, i.e. the enthalpy function remained on the melting or freezing curve, as the case may be, without any transitions. The operator '*nojac*' is used in COMSOL to ensure that the previous solution variables are not included in the solution of the conservation equations for the current time step.

3.3. Annual simulation parameters and boundary conditions

The annual simulation methodology is the same as reported previously [18, 23]. Appropriate exterior and interior boundary conditions are required for the annual simulations. The exterior boundary conditions were estimated using typical meteorological year (TMY3) weather data [41] for Charleston, South Carolina (SC). Input files containing hourly values of outdoor and sky temperatures, solar irradiation and exterior surface convective heat transfer coefficients were generated for the annual simulation models. Eqs. 5 and 6 represent the exterior and interior boundary conditions. In eq. 5, the first term on the right side is the solar irradiance, the second term is the convection heat transfer and the last term is the long-wave radiation (LWR) exchange with the surroundings. Symmetry boundary condition was assumed at the stud and cavity centerlines, i.e. there was no heat flux across those surfaces as represented by eq. 7.

$$q_{ext} = \alpha q_{solar} + h_{ext}(T_{out} - T_{surf}) + \varepsilon\sigma\left[(1 - F_{sky})\left(T_{out}^4 - T_{surf}^4\right) + F_{sky}\left(T_{sky}^4 - T_{surf}^4\right)\right] \quad (5)$$

$$q_{int} = h_{int}(T_{room} - T_{surf}) \quad (6)$$

$$-\mathbf{n} \cdot \mathbf{q} = 0 \quad (7)$$

In the above equations,

α = Solar absorptance of the exterior wall surface, assumed to be 0.6

ε = Infrared emittance of the exterior wall surface, assumed to be 0.8

ent = Exterior surface, facing the conditioned space

int = Interior surface, facing the conditioned space

q = Heat flux (W/m^2)

q = Heat flux vector (W/m^2)

n = Boundary normal vector

q_{solar} = Solar irradiance on the exterior wall surface (W/m^2), from TMY3 data

h_{ext} = Exterior surface convective heat transfer coefficient (W/m^2/K)

h_{int} = Interior surface heat transfer coefficient (W/m^2/K)

F_{sky} = Radiation view factor from sky to the wall

T_{out} = Outside ambient temperature (K), from TMY3 data

T_{sky} = Sky temperature (K), from TMY3 data

T_{surf} = Wall surface temperature (K); exterior wall surface facing the outdoor environment in eq. 5 and interior surface facing the room in eq. 6

T_{room} = Room or interior conditioned space temperature (K)

Hourly values of 'h_{ext}' and 'q_{solar}' for the different wall orientations were generated with the help of EnergyPlus™ [42], a whole-building modeling tool. Values of 'h_{ext}' were calculated using the outdoor temperature and wind velocity data from the TMY3 files. The LWR exchange between the exterior wall surface and the outside, ground and sky can be described by eq. 8. For simplicity, it was assumed that the outside (T_{out}) and ground surface temperatures (T_{ground}) are the same, reducing the LWR exchange to eq. 9. F_{sky}, F_{out} and F_{ground} are the view factors between the exterior wall surface and the sky, outside and ground, respectively. The sum of those three view factors is unity (eq. 10), which results in the LWR term in eq. 5. F_{sky} was calculated using a relation from Walton [43], listed as eq. 11, and it has a value of 0.35 for a vertical wall (ϕ = 90°).

$$q_{LWR} = \varepsilon\sigma\left[F_{out}\left(T_{out}^4 - T_{surf}^4\right) + F_{ground}\left(T_{ground}^4 - T_{surf}^4\right) + F_{sky}\left(T_{sky}^4 - T_{surf}^4\right)\right] \quad (8)$$

$$q_{LWR} = \varepsilon\sigma\left[\left(F_{out} + F_{ground}\right)\left(T_{out}^4 - T_{surf}^4\right) + F_{sky}\left(T_{sky}^4 - T_{surf}^4\right)\right] \quad (9)$$

$$F_{sky} + F_{out} + F_{ground} = 1 \quad (10)$$

$$F_{sky} = \beta[0.5(1 + cos\phi)]; \beta = \sqrt{0.5(1 + cos\phi)} \quad (11)$$

The interior heat transfer coefficient (h_{int}) was assumed to be 8.29 W/m^2/K, following ASHRAE Handbook of Fundamentals [44], for a non-reflective vertical surface. The influence of the heat gains and losses through the wall on the interior room temperature was captured by allowing the room temperature to float between assumed heating and cooling temperature set points. It was also assumed that the heating and cooling systems could instantaneously match the wall-generated heating and cooling loads, so that the room temperature floated between the set points but never went outside that range. The heating and cooling set points were set to 20 and 22.2˚C, respectively, and these set points are quite common in residential and commercial buildings in the U.S. The choice of the PCM FS21R for characterization and modeling is related to the selected cooling set point, since it has been shown that the energy performance of a PCM is dependent on the relation between its melting temperature and the cooling set point [18].

4. RESULTS AND DISCUSSION

In this section, experimental data and the numerical simulation results are presented and discussed. Also included are simulation results of temperature, *H_PCM* and the PCM specific heat that show that the PCM hysteresis model was operating as per expectations.

4.1. HFMA data

As described in sections 2.1 and 2.2, the heat flux transducers within the HFMA plates record voltage signals that are converted to heat flows using calibration factors. The block averages of the voltage signals are also used to determine the length of time needed after each step change in temperature to reach equilibrium. Figure 5 and Figure 6 show the block-averaged voltage readings from one melting test and one freezing test of the PCM FS21R. The legends or labels describing the curves represent the end temperatures after each temperature step change. The step changes were nominally 1˚C. For clarity, only a few curves are shown that correspond to the temperatures close to and within the phase transition range of FS21R.

The heating curves are characterized by a high positive initial reading followed by a steep decline within a few blocks (3-5) to the equilibrium values. However, when melting is occurring, with associated heat absorption by the PCM, the block averages show a slow, gradual decline. In Figure 5, the three curves exhibiting the most prominent melting behavior are indicated by arrows; these curves correspond to the temperature steps ending at 20, 21 and 22˚C, which is expected, since the nominal melting point of FS21R is 20.7˚C. The cooling curves are characterized by a high negative initial reading followed by an increase to the equilibrium values. When freezing occurs, with associated heat release from the PCM, the increase is slow and gradual. However, often the freezing of the PCM is delayed, as seen by the behavior of FS21R at 20˚C in Figure 6. The curve corresponding to 20˚C initially increased to a small negative number (blocks 2-4) before freezing and heat release started, as indicated by the inverted bell shape of the curve between blocks 5 and 30. Again, the three curves representing temperature steps ending at 18, 19 and 20˚C, which exhibited the most prominent freezing behavior, are indicated by arrows. It is interesting to note that the curve corresponding to 18˚C end point (i.e. temperature step 19 to 18˚C) showed a discernibly slower increase in the negative voltage signals than the curve corresponding to 19˚C (i.e. 20 to 19˚C step); in other words the amount of heat released was greater in the 19-18˚C step than the 20-19˚C step. This indicates that the PCM FS21R is a mixture of components with slightly different freezing temperature ranges (21-20 and 19-18˚C).

Figure 7 and Figure 8 show the measured enthalpy curves from duplicate melting and freezing tests, respectively. The temperature range of the measurements was from 10 to 32˚C. Near and within the phase transition range, 1˚C temperature steps were used for improved resolution, but away from the transition range 2˚C temperature steps were used. The measurements from the duplicate tests were within 4% of each other for all temperature steps, except the 18-19˚C step during melting tests for which the difference was 8%. Figure 9 shows the combined melting and freezing enthalpy curves. The enthalpy is assumed to be zero at 10˚C and is 165.7 J/g at 32˚C (based on the melting tests). The phase transition range is about 18 to 22˚C and a hysteresis of 1˚C is observed; melting ended at 22˚C and freezing started at 21˚C. Figure 10 shows the melting and freezing specific heats based on the enthalpy measurements. The specific heat curve during freezing has two peaks, at 18.5 and 20.5˚C, indicating the presence of components with distinct freezing temperatures.

Another PCM, FS29, was tested using the HFMA method. Two tests each were performed for melting and freezing. In this case, rather than duplicating the temperature steps as with FS21R, the temperature steps were offset. The first melting test contained temperature steps of 14-16, 16-18, 18-20, …., 36-38˚C, and the second melting test contained steps of 17-19, 19-21, …., 35-37˚C. Similarly, offset temperature steps were used for the freezing tests. Following the analysis process described in ASTM C1784 [14], the enthalpy data from the different tests were combined and are listed in Table 2. 'T_{start}' and 'T_{end}' are the initial and final temperatures for each temperature step, 'ΔH' is the change in enthalpy during the temperature steps and 'H' is the cumulative enthalpy function. Figure 11 shows the combined enthalpy curves of FS29.

Table 2. Combined melting and freezing enthalpy data of FS29

T_{start} (˚C)	T_{end} (˚C)	ΔH (J/g)	H (J/g)	Remarks
Melting test 1	14		0	
14	16	3.87	3.87	
16	18	4.12	8.00	
18	20	4.46	12.46	
20	22	4.86	17.32	
22	24	6.34	23.67	
24	26	10.42	34.09	
26	28	27.72	61.81	
28	30	74.99	136.80	
30	32	5.61	142.41	
32	34	6.49	148.90	
34	36	6.30	155.19	
36	38	4.48	159.67	
Melting test 2	17		***5.92***	'*H*' interpolated from melting test 1
17	19	4.32	10.24	
19	21	5.06	15.31	
21	23	6.36	21.66	
23	25	***9.65***	31.31	
25	27	22.64	53.95	
27	29	77.10	131.05	
29	31	10.51	141.57	
31	33	5.54	147.10	
33	35	4.17	151.27	
35	37	4.21	155.48	
Freezing test 1	38		***159.67***	'*H*' from melting test 1
38	36	-3.88	155.79	
36	34	-4.01	151.79	
34	32	-3.96	147.82	
32	30	-6.50	141.33	
30	28	-8.06	133.27	
28	27	-43.97	89.30	
27	26	-12.17	77.13	
26	24	-12.97	64.16	
24	22	-8.44	55.72	
22	20	-5.68	50.04	
20	18	-5.06	44.98	
18	16	-4.68	40.31	
16	14	-4.44	35.87	
14	12	-4.66	31.21	

Freezing test 2	35		***153.72***	‘*H*’ interpolated from freezing test 1
35	33	-4.74	148.98	
33	31	-5.00	143.98	
31	29	-5.21	138.76	
29	27	-38.57	100.19	
27	25	-21.94	78.25	
25	23	-9.58	68.67	
23	21	-6.09	62.58	

4.2. Annual simulations with PCM incorporated in an external wall

Annual simulations were performed using the wall model depicted in Figure 4 and using TMY3 weather data for Charleston. The simulations were performed over a period of one year or 8760 hours (365 days x 24 hours) and the variables of interest (temperature, PCM properties, heat flows, etc.) were written in output files on an hourly basis. The first step in the modeling work was to check the validity of the hysteresis model, described in section 3.2, in capturing the phase of the PCM FS21R. To evaluate the hysteresis model, the temperature, the variable *H_PCM* and specific heat ($C_{p,\ PCM}$) were monitored at a point ‘A’ in the PCM layer. The location of point ‘A’ is indicated by the red dot in Figure 12. Figure 13 shows the calculated temperature and *H_PCM* at point ‘A’ as a function of time between the time period of February 22-28; the values of *H_PCM* correspond to the right vertical axis. The selected time period was chosen for illustration due to the frequent switching of the PCM state between melting and freezing enthalpy curves. The thick horizontal, dashed black and green lines correspond the melting end and freezing end temperatures, respectively. When the temperature of the PCM rises above the melting end point (22˚C), the PCM should transition from the melting to the freezing curve, and vice-versa when the PCM temperature drops below the freezing end point (18˚C). A value of zero of *H_PCM* is associated with the melting curve and a value of one is associated with the freezing curve. As observed in Figure 13, while the temperature remained below 22˚C, the value of *H_PCM* was zero. In the simulations, at 5 PM on February 22, the temperature rose above 22˚C and *H_PCM* switched to a value of one. *H_PCM* remained at one till the temperature dropped below 18˚C at 8 AM on February 25, when it switched back to zero. Subsequently, *H_PCM* switched between zero and one whenever the temperature crossed the melting and freezing end points.

Figure 14 shows the calculated PCM specific heat (‘Cp - PCM’, based on the value of *H_PCM*) and specific heats based on the melting and freezing curves (‘Cp - Melting’ and ‘Cp - Freezing’). The transition of $C_{p,\ PCM}$ between the melting and freezing curves are clearly observable; the transitions are marked by thin vertical black, dashed lines. The times of these transitions coincide with the switching of the values of *H_PCM*. At 5 PM on February 22, the $C_{p,\ PCM}$ transitioned from the melting to the freezing curve as *H_PCM* went from zero to one; on February 25, 8 AM, *H_PCM* went from one to zero and $C_{p,\ PCM}$ transitioned from the freezing to the melting curve, and so on. Thus, the hysteresis model accurately captured the shift of the PCM enthalpy between melting and freezing enthalpy curves depending on the temperature within the PCM layer.

Next, annual simulations were performed with three different scenarios: (i) baseline model without the PCM (‘No PCM’), (ii) model with the PCM layer, but the PCM specific heat (C_p) based on the melting enthalpy curve alone (‘Hmelt’), and (iii) model with PCM hysteresis, i.e. $C_{p,\ PCM}$ is based on both melting and freezing enthalpy curves depending on the value of *H_PCM* (‘Hmelt/freeze’). The main quantity of interest is the heat transfer at the interior wall surface, which is facing the room. The heat gains and losses at this surface represent the wall-generated loads that need to be compensated by mechanical heating or cooling to maintain the indoor comfort conditions. The simulations were performed for a south-oriented wall, which typically experiences the highest heat gains in Charleston. Further, the analysis of the simulation results is focused on heat gains and resultant cooling energy use, since Charleston is in a warm, humid climate zone.

To illustrate the PCM behavior, Figure 15 shows the calculated spatially-averaged temperature and specific heat within the PCM layer. The results are shown for typical 2-day periods during spring (April 28 – 29) and summer (July 17-18) in Charleston. During the spring period (Figure 15(a)), for a majority of the time, the calculated temperature in the melting curve only case ('Hmelt') remained within the PCM transition range (i.e. below the melting end point of 22°C) and the specific heat ($C_{p,PCM}$ (Hmelt)) remained at a high level (> 20 J/g/K). During the late-afternoon of April 29, the temperature rose above 22°C and the $C_{p,PCM}$ (Hmelt) decreased to about 1.8 J/g/K, which indicates the fully-molten regime. When hysteresis was included in the model ('Hmelt/freeze'), the temperature rose above 22°C during the afternoons on both spring days and the $C_{p,PCM}$ (Hmelt/freeze) decreased to fully-molten value of 1.8 J/g/K. Thus, including hysteresis clearly impacts the calculations of PCM behavior. During the summer days (Figure 15(b)), the calculated temperatures were predominantly above 22°C and the $C_{p,PCM}$ from both the 'Hmelt' and 'Hmelt/freeze' cases remained in the 1.8-2.1 J/g/K range, except briefly during the early hours of July 17.

Figure 16 compares the calculated heat flows per unit wall area at the interior wall surface for the 'No PCM', 'Hmelt' and 'Hmelt/freeze' cases. Positive heat flows represent internal heat gains and negative flows represent heat losses. The impact of the PCM layer during spring is clearly visible in Figure 16(a), with reduced heat gains and no heat losses compared to the baseline case ('No PCM'). Also evident is the difference in the calculated heat flows when the

PCM hysteresis is ignored (‘Hmelt’) or captured (‘Hmelt/freeze’). The differences in the calculated heat flows under the ‘Hmelt’ and ‘Hmelt/freeze’ cases follow the $C_{p,PCM}$ profiles in Figure 15(a). In the ‘Hmelt’ case, the heat gains were zero at all times when $C_{p,PCM}$ (Hmelt) remained above 20 J/g/K; the heat gains rose to 3 W/m^2 during late afternoon on April 29, when the PCM was fully molten and $C_{p,PCM}$ (Hmelt) decreased to 1.8 J/g/K. Conversely, $C_{p,PCM}$ (Hmelt/freeze) decreased to 1.8 J/g/K during the afternoons of both April 28 and 29, and peak heat gains of about 5.5 W/m^2 were observed during both days. During summer (Figure 16(b)), the PCM in both the ‘Hmelt’ and ‘Hmelt/freeze’ cases was in a predominantly fully-molten state and was not benefitting from the phase transitions and latent heat storage; hence, no discernible difference was observed in the heat gains from the two PCM cases. The slight reduction in the peak heat gains compared to the ‘No PCM’ case is presumably resulting from the added thermal resistance of the molten PCM layer.

In order to further evaluate the impact of the degree of hysteresis on PCM performance, additional scenarios were considered using assumed freezing enthalpy curves with additional hysteresis. Figure 17 shows the measured (‘F_Meas’) and assumed enthalpy curves for freezing; ‘F_H2C’ and ‘F_H4C’ represent the freezing curves with additional hysteresis of 2 and 4˚C, respectively. ‘F_H2C’ and ‘F_H4C’ were created by shifting the measured freezing enthalpy curve by 2 and 4˚C to lower temperatures.

Figure 18 shows the calculated monthly-integrated heat gains per unit wall area through a south-facing wall for all the scenarios modeled, without and with PCM as well as using different enthalpy curves and degrees of hysteresis to define the PCM specific heat. The reductions in heat gains with the PCM layer are most significant during the non-summer months (January-May and October-December). During these months, the impact of using one (‘Hmelt’) vs. two enthalpy curves (‘Hmelt/freeze’) and additional hysteresis (‘Hmelt/f_H2C’ and ‘Hmelt/f_H4C’) on the calculated heat gains are clearly observable. The calculated heat gains are minimum when the PCM specific heat is defined by the melting enthalpy curve only, and progressively increase when both melting and freezing enthalpy curves are used and with increasing degrees of hysteresis. During summer (June-September), the heat gains are almost identical regardless of the enthalpy curves used to define the specific heat; this is presumably due to the PCM layer being predominantly molten during this time and not benefitting from phase transitions.

To get a better sense of the resulting cooling energy consumption, the calculated heat gains were converted to electricity consumption using temperature-dependent coefficients of performance (COP) of a typical heat pump unit, following [18]. The COP of the heat pump is a function of the ambient temperature. Since the cooling equipment is often placed in an unconditioned space, it operates more efficiently when the outside temperatures are lower. This adds to the potential for cooling energy savings since PCMs enable delayed heat gains through walls compared to walls without PCM, as seen in Figure 16.

Table 3 shows the variation of the heat pump COP with outside temperature. The hourly calculated heat gains were converted to electricity consumption using the COP values listed in table 3; linear interpolation was used to estimate COP values at outdoor temperatures other than those listed in table 3. It was assumed that the cooling equipment operated only when the room temperature tended to exceed the cooling set point (22.2˚C). In other words, if the room temperature remained below the cooling set point, the electricity consumption was set to zero even if there was some heat gain through the walls. This was done to differentiate between cooling loads in summer and heat gains in winter (or spring/autumn); the latter might offset the heating energy needs and do not add to the cooling energy use.

Table 3. Temperature-dependent heat pump COP

Outdoor temperature (˚C)	COP (Wh/Wh)
23.89	4.16
29.44	3.73
35.00	3.22
40.56	2.72
46.11	2.28

Table 4 shows the calculated annual heat gains per unit wall area and resultant cooling electricity consumption for the different scenarios considered. Again, the impact of the PCM layer in reducing heat gains and electricity consumption are clearly observable. Further, when utilizing both melting and freezing enthalpy curves in the model, the savings are discernibly lower than when using the melting curve alone, 29% vs. 32%, respectively. With PCMs that exhibit significant hysteresis, the savings can be expected to be significantly lower than with PCMs that show little to no hysteresis. For the current wall configuration and climate zone, the PCMs with added hysteresis (‘Hmelt/f_H2C’ and ‘Hmelt/f_H4C’) were estimated to save only 12-15% in cooling electricity compared to 29% with the actual PCM, FS21R, which is represented by ‘Hmelt/freeze’.

Table 4. Comparison of calculated annual heat gains per unit wall area and cooling electricity use between different modeled scenarios

	Annual heat gain (Wh/m^2)	% Difference	Annual electricity (Wh/m^2)	% Difference
No PCM	22507		5601	
Hmelt	14609	-35.1	3813	-31.9
Hmelt/freeze	15284	-32.1	3969	-29.1
Hmelt/f_H2C	18962	-15.7	4772	-14.8
Hmelt/f_H4C	19674	-12.6	4912	-12.3

5. SUMMARY, CONCLUSIONS AND FUTURE WORK

Temperature-dependent enthalpy functions of two fatty-acid based PCM products, FS21R and FS29, were measured using a heat flow meter apparatus (HFMA). The measurements were done according to ASTM C1784, a standard test method for thermal characterization of full-scale PCM products. The measured enthalpy functions of FS21R were utilized in a 2D wall model. The model incorporated a hysteresis model to include both melting and freezing enthalpy curves with varying degrees of hysteresis. Simulations were performed for a south-oriented wall in Charleston, SC using typical yearly climate data. Hourly heat gains through the wall and associated cooling electricity consumption were calculated for different scenarios: (i) baseline wall without the PCM layer, (ii) wall with the PCM layer, but the PCM specific heat based on the melting enthalpy curve alone, and (iii) PCM specific heat based on the melting and freezing enthalpy curves and with varying degrees of hysteresis.

The results showed that including the hysteresis effect significantly impacts the calculated thermal performance of the PCM layer and resultant energy savings compared to a wall without the PCM. For the current wall model, orientation (south-facing wall) and climate conditions, simulations with the PCM specific heat based on only the melting enthalpy curve showed 32% reduction in the wall-related cooling electricity consumption. The calculated energy savings dropped to 29% when both the melting and freezing enthalpy curves are used; the calculated savings were further reduced to 15% and 12% when additional 2-4˚C of hysteresis between the melting and freezing enthalpy curves were assumed.

A significant assumption in the numerical simulations was related to the treatment of hysteresis and interrupted melting or freezing. Here, it was assumed that the PCM state remained on the same enthalpy curve even if the melting or freezing was interrupted, and only transitioned to the other curve if the temperature went above or below the melting and freezing end points, respectively. It will interesting to evaluate the difference in the calculated PCM performance if instantaneous transition to the melting curve was allowed in case of interrupted freezing (or vice-versa), as has been done in some studies. Another important next step is to couple the 2D wall model to a whole-building energy analysis software to determine the impacts of PCMs, with and without hysteresis, on the whole-building energy performance.

6. ACKNOWLEDGEMENTS

The U.S. Department of Energy (DOE) and the Department of Science and Technology (DST), Government of India (GOI) provided joint funding for this work, which was performed under the U.S.–India Partnership to Advance Clean Energy Research (PACE-R) program's "U.S.–India Joint Center for Building Energy Research and Development" (CBERD) project. Funding for the research work done by Oak Ridge National Laboratory was provided by the U.S. DOE and the authors wish to thank Dr. Karma Sawyer and Mr. Sven Mumme for their guidance and support. The DST, GOI, administered by Indo-U.S. Science and Technology Forum, supported the India-side research activity. The authors also acknowledge the support from Pluss Advanced Technologies, in providing PCM tiles for the HFMA measurements. Finally, thanks to COMSOL Technical Support for their help in resolving modeling-related issues.

7. REFERENCES

1. Zalba B, Marín JM, Cabeza LF, Mehling H. Review on thermal energy storage with phase change: materials, heat transfer analysis and applications. Applied Thermal Engineering. 2003;23(3):251-83.
2. Souayfane F, Fardoun F, Biwole PH. Phase change materials (PCM) for cooling applications in buildings: A review. Energy and Buildings, 2016;129:396-431.

3. Akeiber H, Nejat P, Majid MZ, Wahid MA, Jomehzadeh F, Famileh IZ, Calautit JK, Hughes BR, Zaki SA. A review on phase change material (PCM) for sustainable passive cooling in building envelopes. Renewable and Sustainable Energy Reviews, 2016;60:1470-97.

4. Yinping Z, Yi J. A simple method, the-history method, of determining the heat of fusion, specific heat and thermal conductivity of phase-change materials. Measurement Science and Technology, 1999;10(3):201.

5. Marín JM, Zalba B, Cabeza LF, Mehling H. Determination of enthalpy–temperature curves of phase change materials with the temperature-history method: improvement to temperature dependent properties. Measurement science and technology, 2003;14(2):184.

6. Arkar C, Medved S. Influence of accuracy of thermal property data of a phase change material on the result of a numerical model of a packed bed latent heat storage with spheres. Thermochimica Acta, 2005;438(1):192-201.

7. Günther E, Hiebler S, Mehling H, Redlich R. Enthalpy of phase change materials as a function of temperature: required accuracy and suitable measurement methods. International Journal of Thermophysics, 2009;30(4):1257-69.

8. Castellón C, Günther E, Mehling H, Hiebler S, Cabeza LF. Determination of the enthalpy of PCM as a function of temperature using a heat-flux DSC—A study of different measurement procedures and their accuracy. International Journal of Energy Research, 2008;32(13):1258-65.

9. Marín JM, Zalba B, Cabeza LF, Mehling H. Determination of enthalpy–temperature curves of phase change materials with the temperature-history method: improvement to temperature dependent properties. Measurement Science and Technology,

2003;14(2):184

10. Sandnes B, Rekstad J. Supercooling salt hydrates: stored enthalpy as a function of temperature. Solar Energy, 2006;80(5):616-25.

11. Kravvaritis ED, Antonopoulos KA, Tzivanidis C. Improvements to the measurement of the thermal properties of phase change materials. Measurement Science and Technology, 2010;21(4):045103.

12. Solé A, Miró L, Barreneche C, Martorell I, Cabeza LF. Review of the T-history method to determine thermophysical properties of phase change materials (PCM). Renewable and Sustainable Energy Reviews, 2013 Oct 31;26:425-36.

13. D'Avignon K, Kummert M. Assessment of T-history method variants to obtain enthalpy–temperature curves for phase change materials with significant subcooling. Journal of Thermal Science and Engineering Applications, 2015;7(4):041015.

14. ASTM C1784-14. 2014. Standard Test Method for Using a Heat Flow Meter Apparatus for Measuring Thermal Storage Properties of Phase Change Materials and Products. ASTM International, West Conshohocken, PA, USA.

15. Kim HB, Mae M, Choi Y. Application of shape-stabilized phase-change material sheets as thermal energy storage to reduce heating load in Japanese climate. Building and Environment, 2017;125:1-4.

16. Zhou G, Zhang Y, Wang X, Lin K, Xiao W. An assessment of mixed type PCM-gypsum and shape-stabilized PCM plates in a building for passive solar heating. Solar Energy, 2007;81:1351-60.

17. Kara YA. Diurnal performance analysis of phase change material walls. Applied Thermal Engineering, 2016;102:1-8.

18. Biswas K, Lu J, Soroushian P, Shrestha S. Combined experimental and numerical evaluation of a prototype nano-PCM enhanced wallboard. Applied Energy, 2014;131:517-29.

19. Hawes DW, Feldman D. Absorption of phase change materials in concrete. Solar Energy Mater Solar Cells, 1992;27:91–101.

20. Vicente R, Silva T. Brick masonry walls with PCM macrocapsules: An experimental approach. Applied Thermal Engineering, 2014;67:24-34.

21. Shrestha S, Miller W, Stovall T, Desjarlais A, Childs K, Porter W, et al. Modeling PCM-enhanced insulation system and benchmarking EnergyPlus against controlled field data. Proc. Building Simulation 2011: 12th Conf. International Building Performance Simulation Association, p 800-7, 2011, available online at http://www.ibpsa.org/proceedings/BS2011/P_1328.pdf.

22. Serrano A, Borreguero AM, Garrido I, Rodríguez JF, Carmona M. Reducing heat loss through the building envelope by using polyurethane foams containing thermoregulating microcapsules. Applied Thermal Engineering. 2016;103:226-32.

23. Biswas K, Abhari R. Low-cost phase change material as an energy storage medium in building envelopes: experimental and numerical analyses. Energy Conversion and Management, 2014;88:1020-31.

24. Kosny J, Biswas K, Miller W, Kriner S. Field thermal performance of naturally ventilated solar roof with PCM heat sink. Solar Energy, 2012;86:2504-14.

25. Biswas K. Nano-based phase change materials for building energy efficiency. Start-Up Creation: The Smart Eco-efficient Built Environment, 2016:183, http://dx.doi.org/10.1016/B978-0-08-100546-0.00009-1.

26. ASTM C518-10. 2010. Standard Test Method for Steady-State Thermal Properties by Means of the Heat Flow Meter Apparatus. ASTM International, West Conshohocken, PA, USA.

27. Shukla N, Kosny J. DHFMA Method for Dynamic Thermal Property Measurement of PCM-integrated Building Materials. Current Sustainable/Renewable Energy Reports, 2015;2(2):41-6.

28. AL-Saadi SN, Zhai ZJ. Modeling phase change materials embedded in building enclosure: A review. Renewable and Sustainable Energy Reviews, 2013;21:659-73.

29. Bony J, Citherlet S. Numerical model and experimental validation of heat storage with phase change materials. Energy and Buildings, 2007;39(10):1065-72.

30. Kenfack F, Bauer M. Innovative Phase Change Material (PCM) for heat storage for industrial applications. Energy Procedia, 2014;46:310-6.

31. Kuznik F, Virgone J. Experimental investigation of wallboard containing phase change material: Data for validation of numerical modeling. Energy and Buildings, 2009;41(5):561-70.

32. Gowreesunker BL, Tassou SA. Effectiveness of CFD simulation for the performance prediction of phase change building boards in the thermal environment control of indoor spaces. Building and Environment, 2013;59:612-25.

33. Delcroix B, Kummert M, Daoud A. Development and numerical validation of a new model for walls with phase change materials implemented in TRNSYS. Journal of Building Performance Simulation, 2017;10(4):422-37

34. Rose J, Lahme A, Christensen NU, Heiselberg P, Hansen M, Grau K. Numerical method for calculating latent heat storage in constructions containing phase change material. In

Eleventh International IBPSA Conference 2009 Jul 27 (pp. 400-407), available online at http://www.ibpsa.org/proceedings/bs2009/bs09_0400_407.pdf

35. Fateh A, Klinker F, Brütting M, Weinläder H, Devia F. Numerical and experimental investigation of an insulation layer with phase change materials (PCMs). Energy and Buildings, 2017;153:231-40.

36. FOX 314 Heat Flow Meter, TA Instruments, http://www.tainstruments.com/fox-314/.

37. NIST SRM 1450, Energy and Environment Division, NIST, https://www.nist.gov/energy-and-environment-division/nist-srm-1450.

38. Tleoubaev A, Brzezinski A, Braga LC. Accurate Simultaneous Measurements of Thermal Conductivity and Specific Heat of Rubber, Elastomers, and Other Materials, *for the 12th Brazilian Rubber Technology Congress*, 2008, available online at http://www.tainstruments.com/pdf/literature/Accurate%20Simultaneous%20Measurements%20of%20Thermal%20Conductivity%20and%20Specific%20Heat.pdf.

39. COMSOL Multiphysics®, Heat Transfer Module, https://www.comsol.com/heat-transfer-module.

40. Using the Previous Solution Operator in Transient Modeling, COMSOL Multiphysics®, https://www.comsol.com/blogs/using-the-previous-solution-operator-in-transient-modeling/.

41. National Solar Radiation Data Base, 1991- 2005 Update: Typical Meteorological Year 3, http://rredc.nrel.gov/solar/old_data/nsrdb/1991-2005/tmy3/.

42. EnergyPlus, https://energyplus.net/.

43. Walton, G.N., 1983. Thermal Analysis Research Program Manual, NBSSIR 83-2655, National Bureau of Standards.

44. ASHRAE Handbook of Fundamentals, 2005, Table 1 – Surface conductances and resistances for air, page 25.2, https://www.ashrae.org/resources--publications/handbook.

LIST OF FIGURES

both melting and freezing curves to calculate Cp,PCM (‘Hmelt/freeze’).

Figure 16. Comparison of calculated internal heat flows without the PCM layer (‘No PCM’), using only the melting curve (‘Hmelt’), and using both melting and freezing curves (‘Hmelt/freeze’); Calculation results are shown for (a) spring and (b) summer periods.

Figure 17. Enthalpy curves for freezing as measured (‘F_Meas.’) and assuming additional hysteresis (‘F_H2C’ and ‘F_H4C’).

Figure 18. Comparison of the total calculated monthly heat gains under the different scenarios: No PCM, Cp,PCM defined by melting curve only (Hmelt), Cp,PCM from melting and freezing curves (Hmelt/freeze), and accounting for additional PCM hysteresis (H2C and H4C).

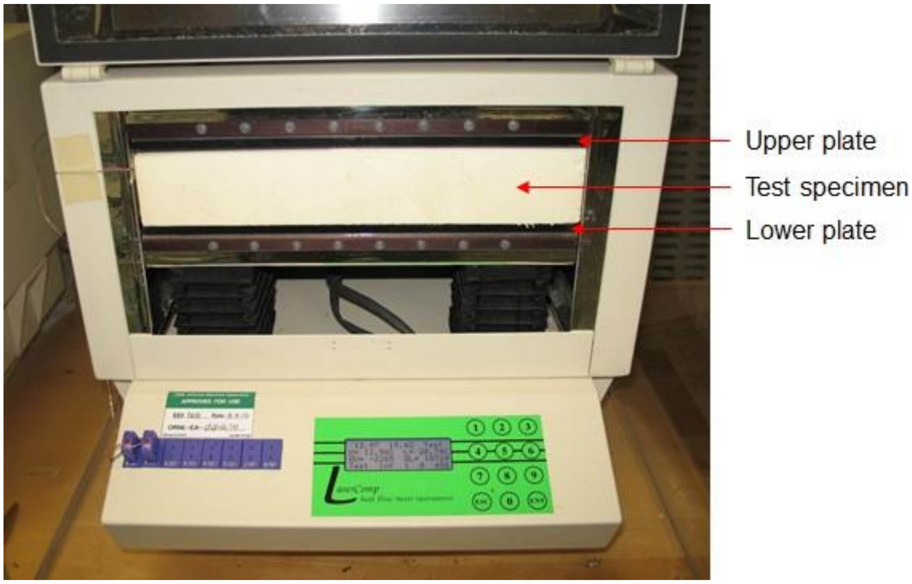

Figure 1. Heat flow meter apparatus used for PCM characterization.

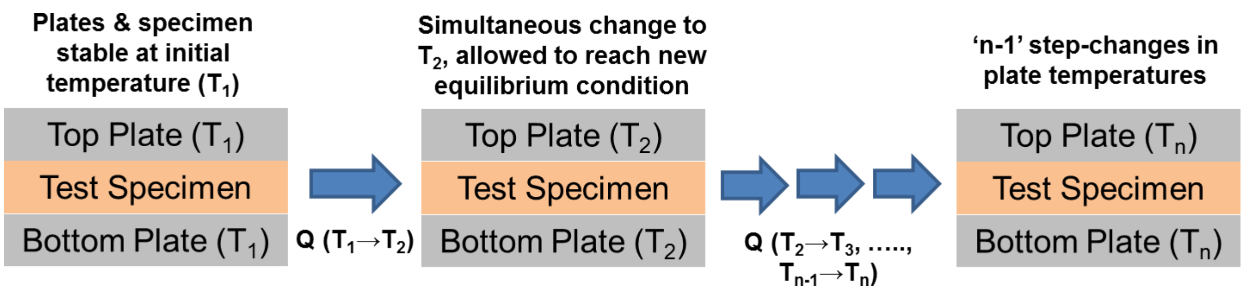

Figure 2. Schematic representation of the PCM characterization method.

Figure 3. PCM FS21R.

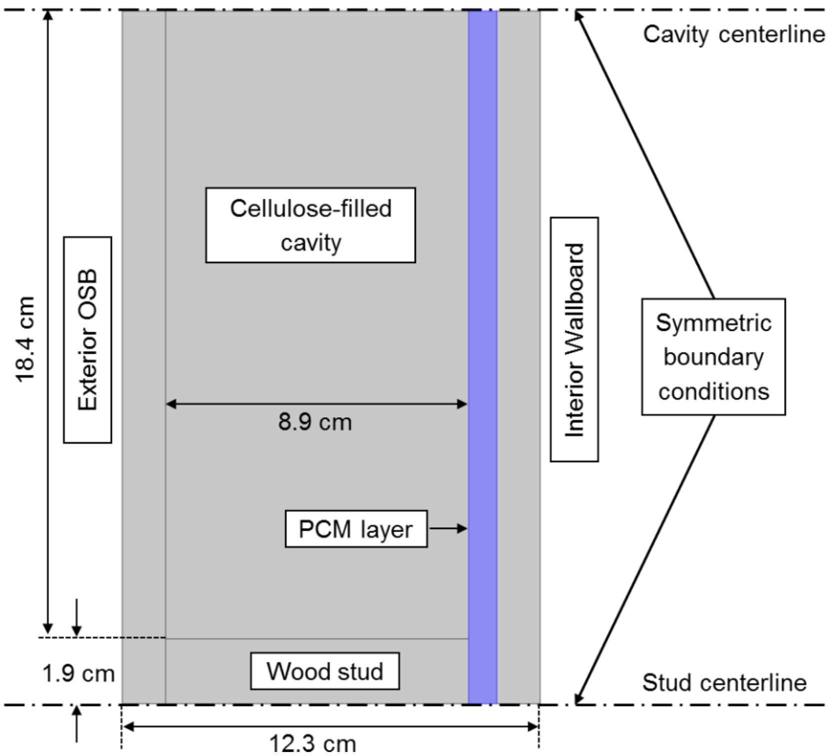

Figure 4. Wall model used in the simulations.

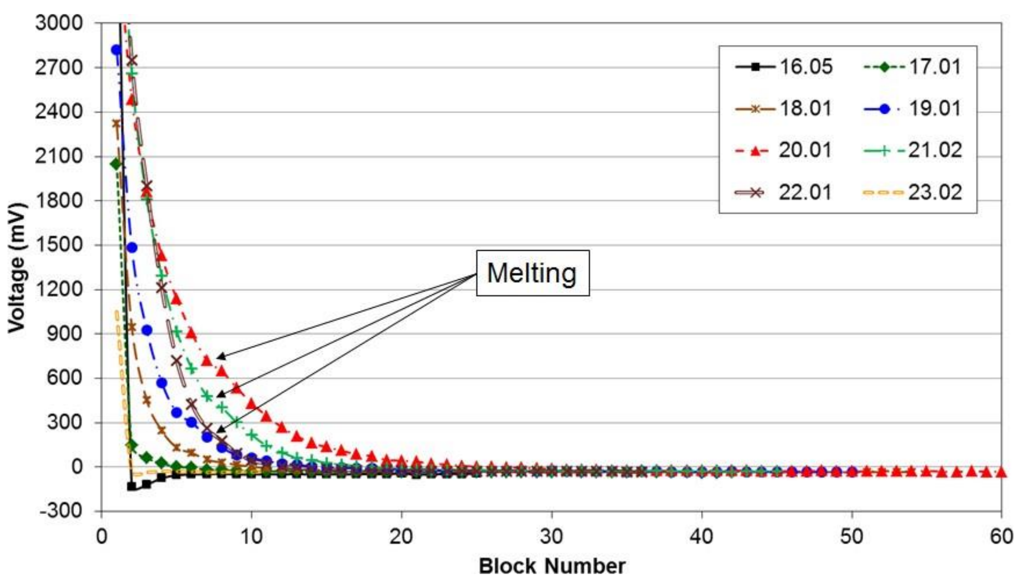

Figure 5. Block-averaged voltage readings from a melting test of FS21R.

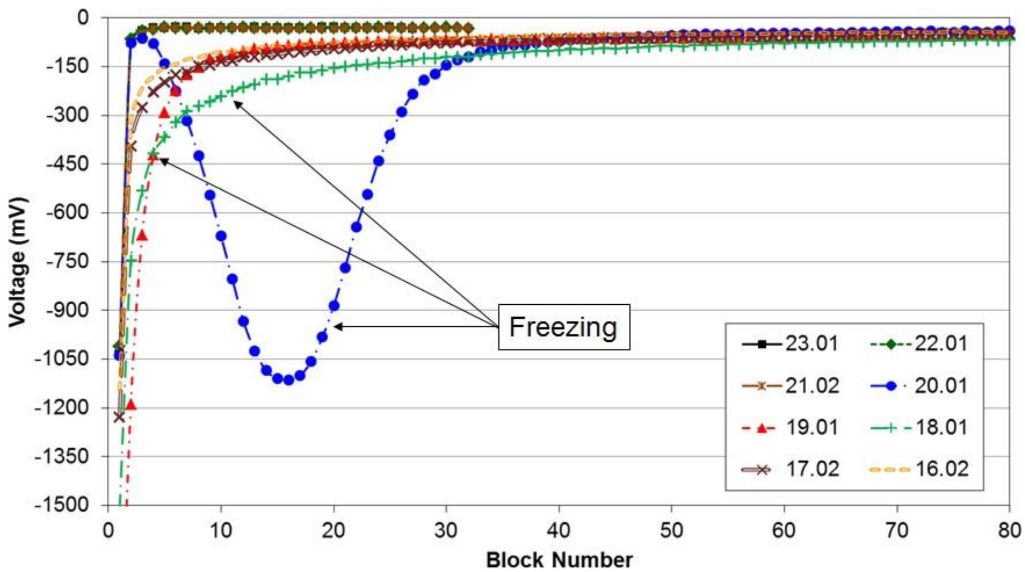

Figure 6. Block-averaged voltage readings from a freezing test of FS21R.

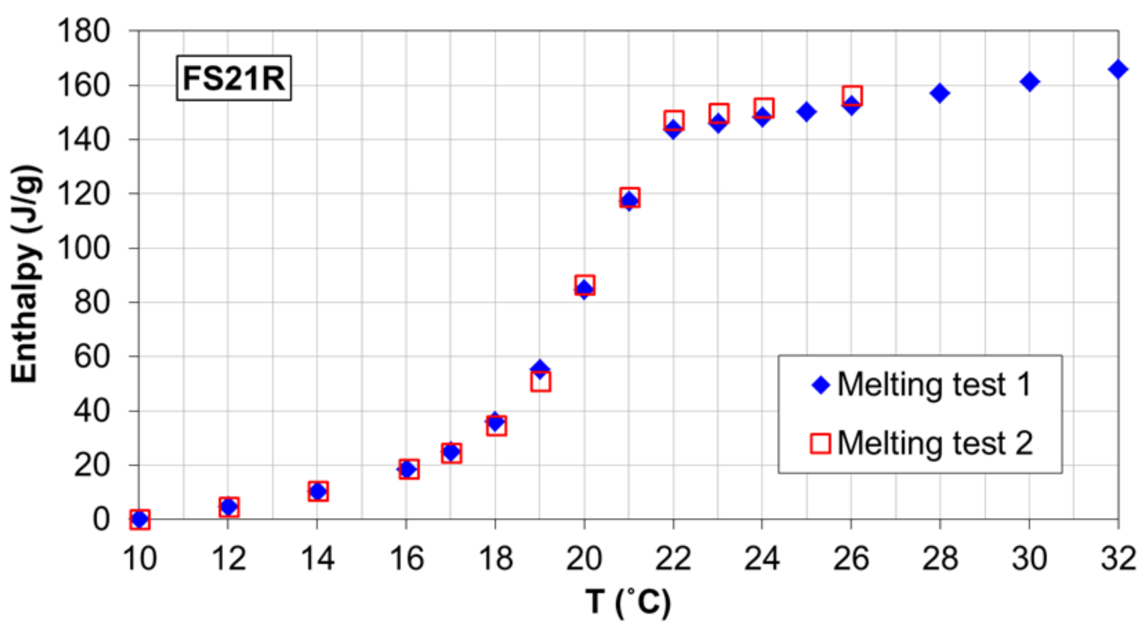

Figure 7. Measured enthalpy of FS21R during melting tests.

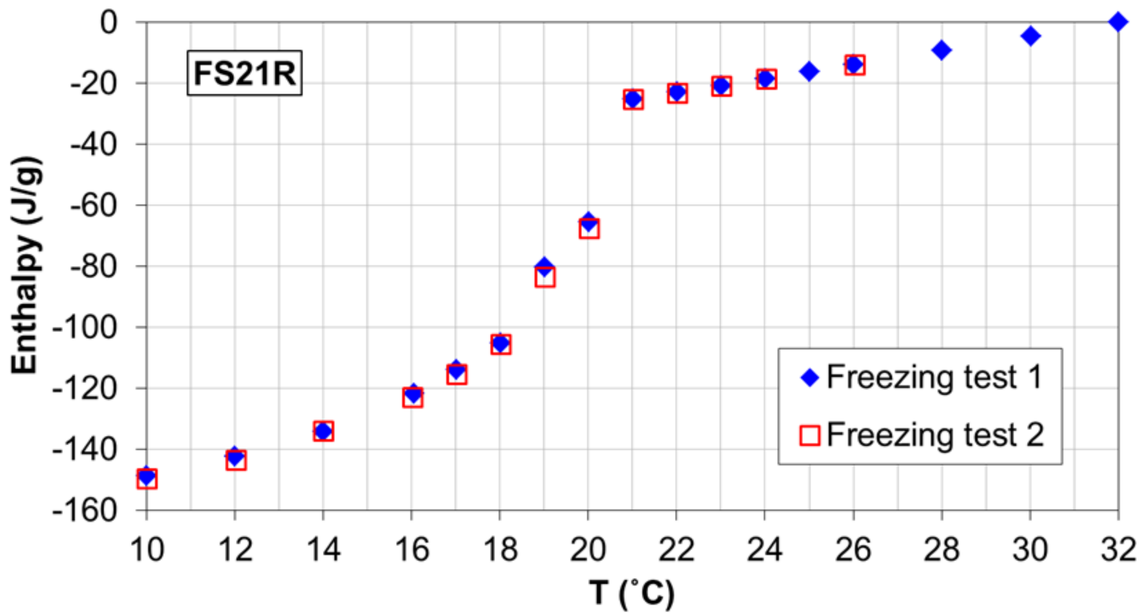

Figure 8. Measured enthalpy of FS21R during freezing tests.

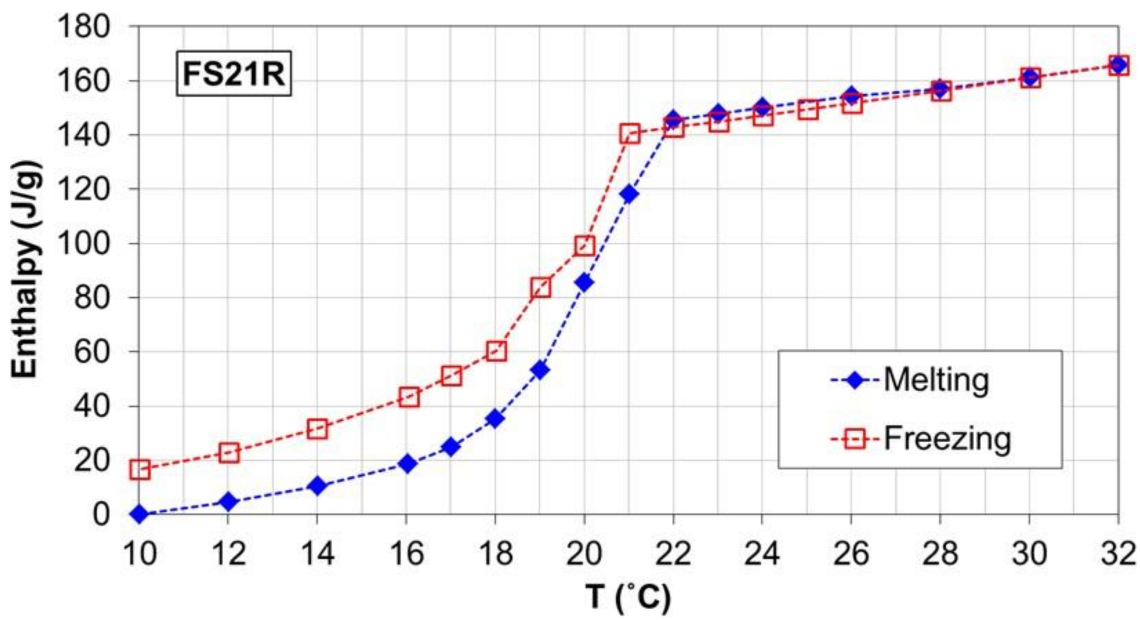

Figure 9. Combined melting-freezing enthalpy functions of FS21R, assuming H = 0 at 10˚C and H = 165.7 J/g at 32˚C.

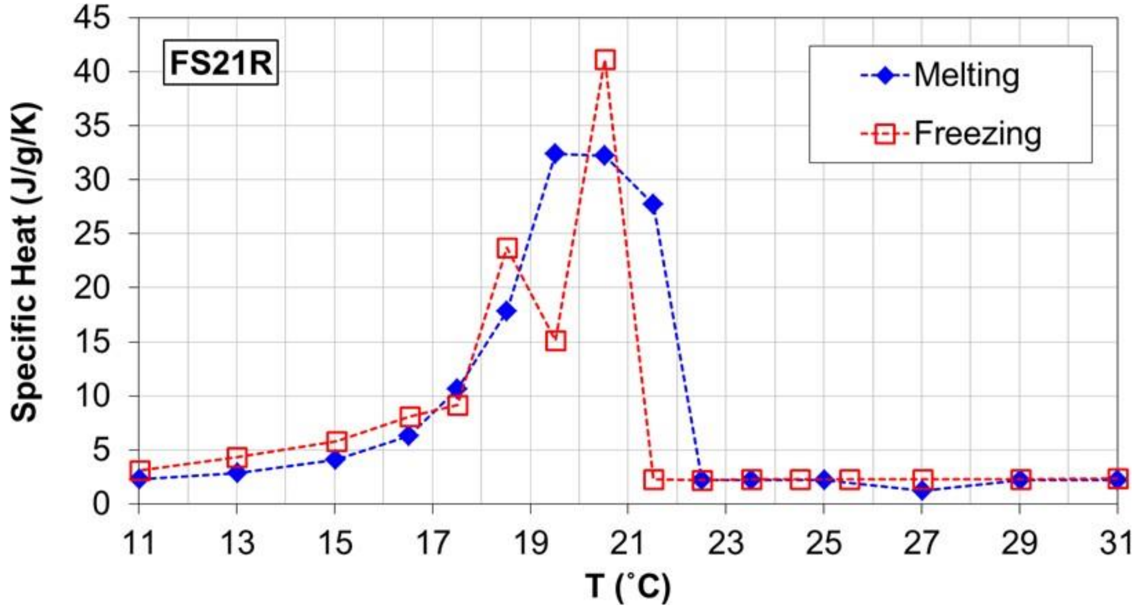

Figure 10. Melting and freezing specific heat functions of FS21R.

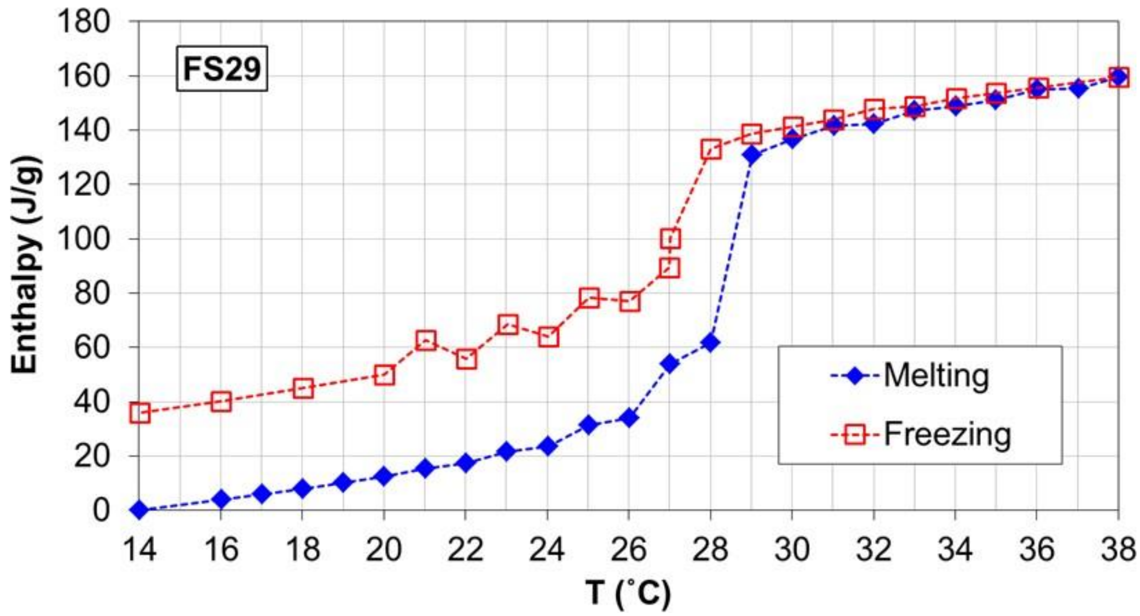

Figure 11. Combined melting-freezing enthalpy functions of FS29, assuming *H* = 0 at 14˚C and *H* = 159.7 J/g at 38˚C.

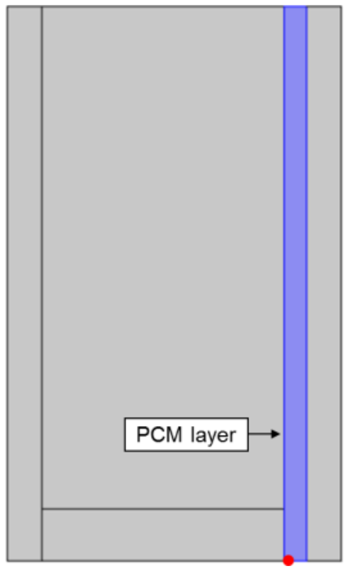

Figure 12. Point 'A' within the PCM layer is indicated by the red dot.

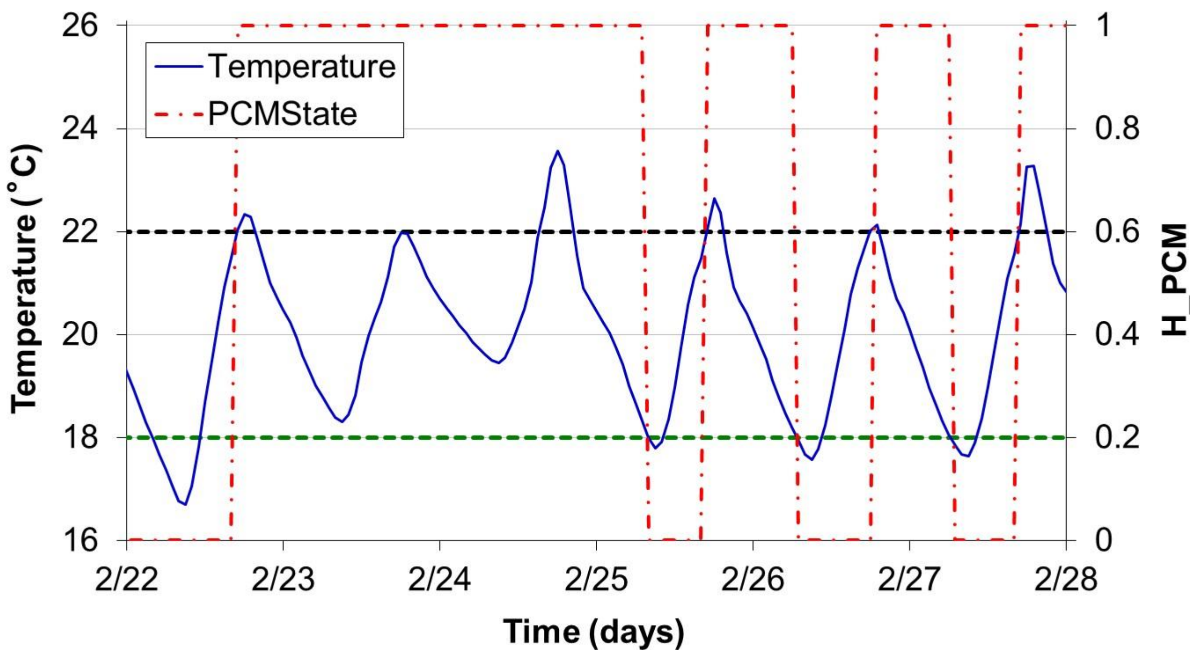

Figure 13. Calculated temperature and *H_PCM* at location 'A' in the PCM domain.

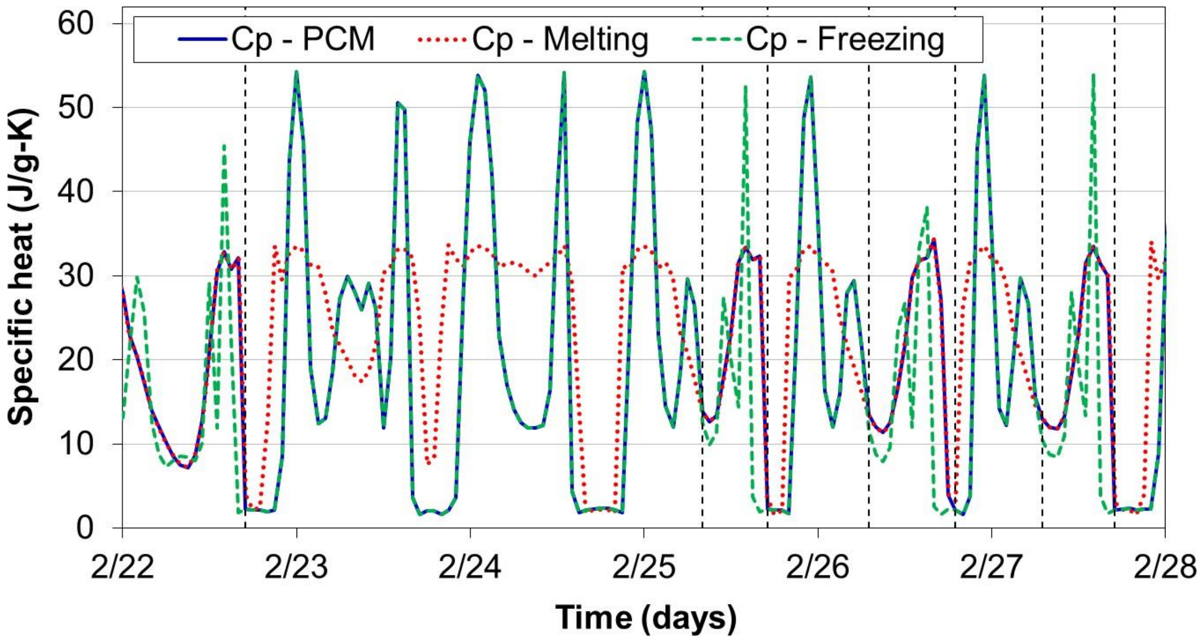

Figure 14. Calculated specific heat (C_p) of the PCM at location 'A' with respect to specific heats based on the melting and freezing enthalpy curves; vertical, dashed blank lines indicate the times at which the C_p shifts from melting to freezing curve and vice-versa.

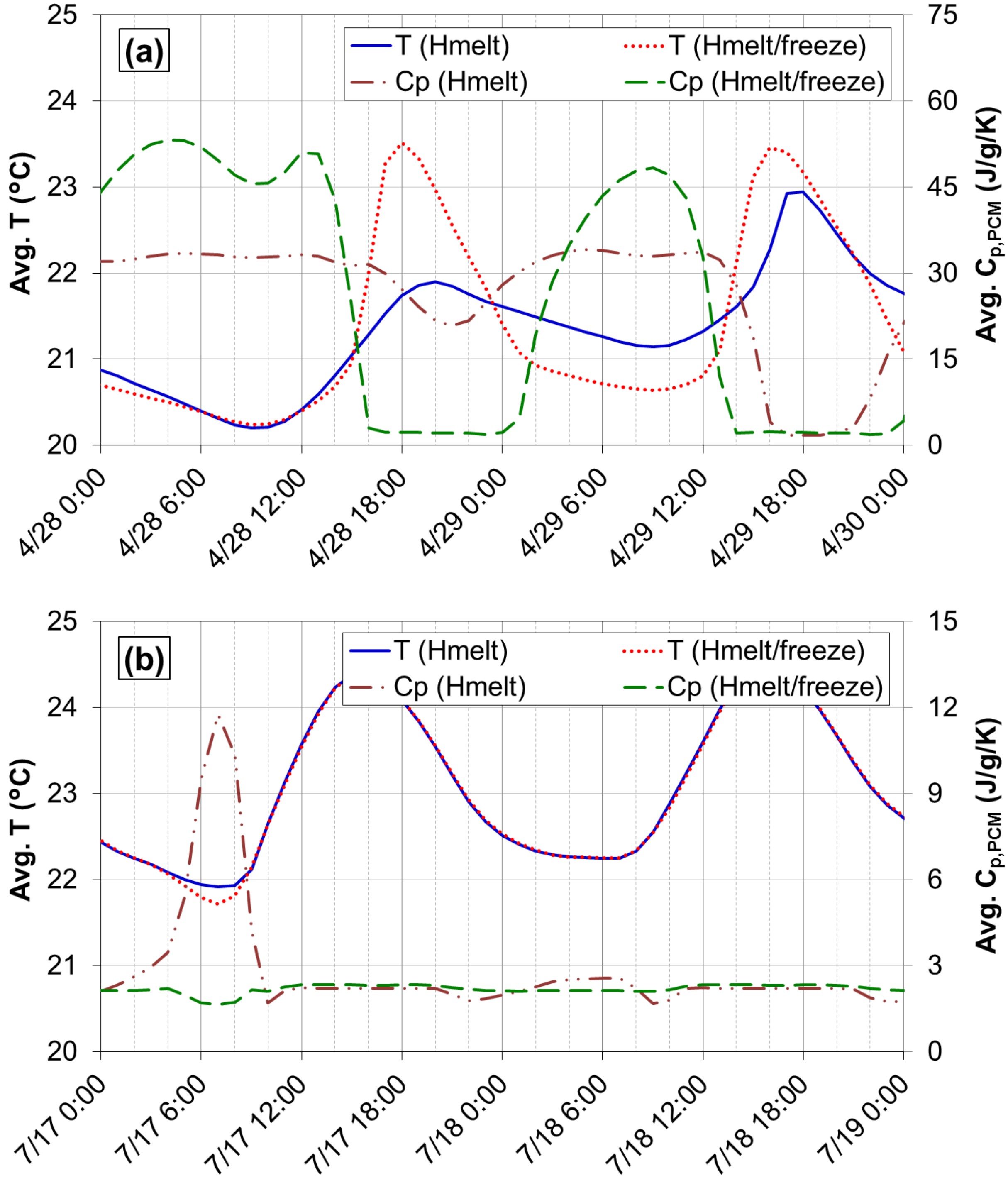

Figure 15. Calculated, spatially-averaged temperature (left axis) and specific heat (right axis) in the PCM layer during (a) spring and (b) summer periods. Results are shown for two cases: (i) assuming only the melting curve defines $C_{p,PCM}$ ('Hmelt'), and (ii) using both melting and freezing curves to calculate $C_{p,PCM}$ ('Hmelt/freeze').

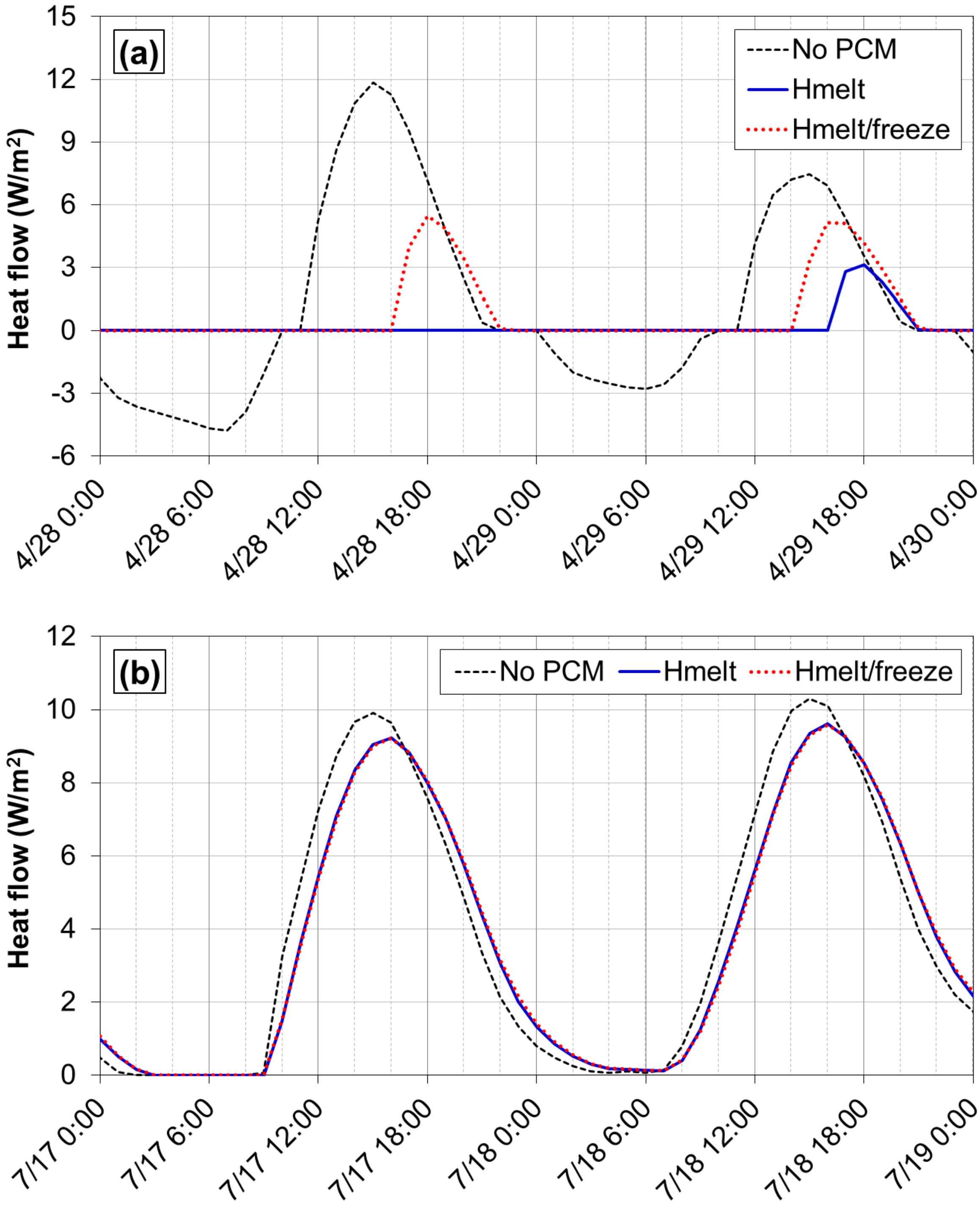

Figure 16. Comparison of calculated internal heat flows without the PCM layer ('No PCM'), using only the melting curve ('Hmelt'), and using both melting and freezing curves ('Hmelt/freeze'); Calculation results are shown for (a) spring and (b) summer periods.

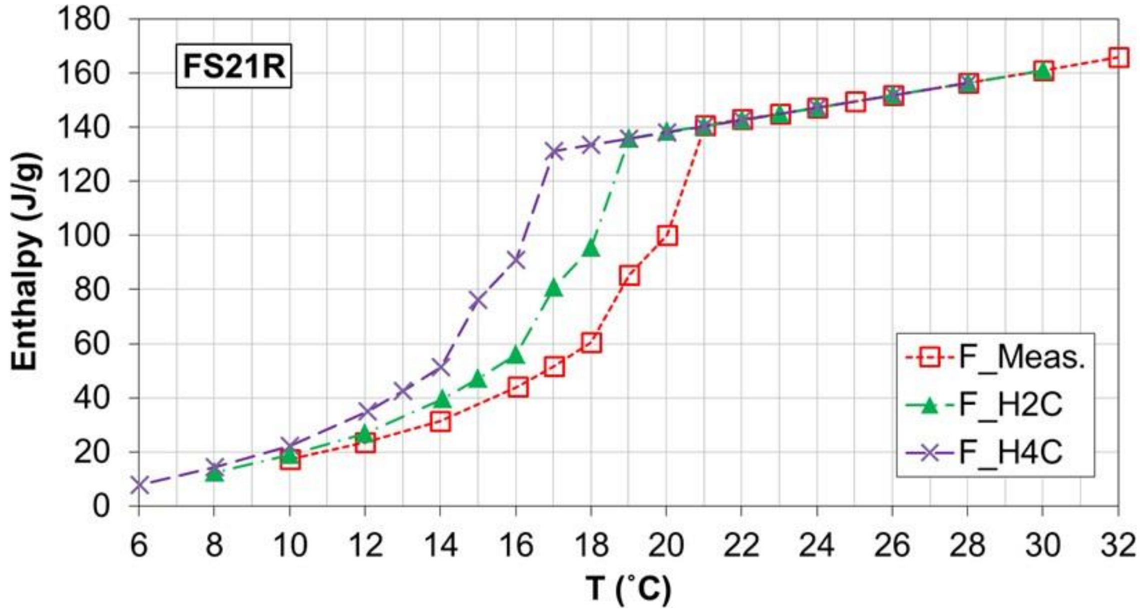

Figure 17. Enthalpy curves for freezing as measured ('F_Meas.') and assuming additional hysteresis ('F_H2C' and 'F_H4C').

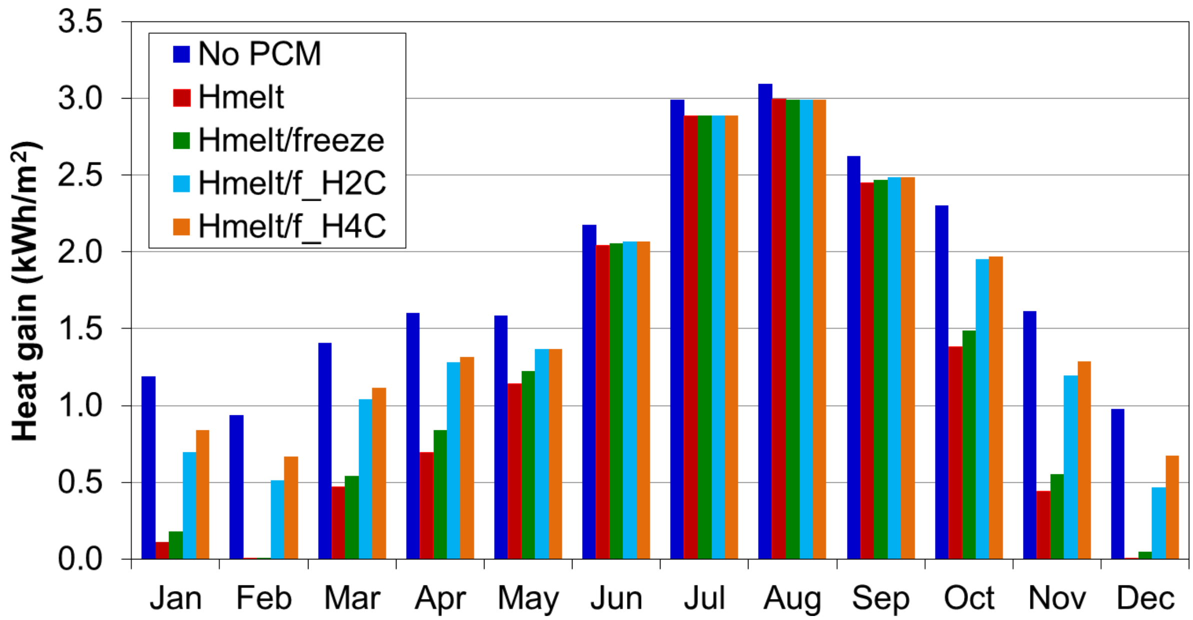

Figure 18. Comparison of the total calculated monthly heat gains under the different scenarios: No PCM, $C_{p,PCM}$ defined by melting curve only (Hmelt), $C_{p,PCM}$ from melting and freezing curves (Hmelt/freeze), and accounting for additional PCM hysteresis (H2C and H4C).